Volume 1 | Number 1 | Jan 2013 | Pages 1–100

Nanoscale

www.rsc.org/nanoscale

ROYAL SOCIETY OF CHEMISTRY

ROYAL SOCIETY OF CHEMISTRY

www.rsc.org/nanoscale

Control of nanoparticle formation using the constrained dewetting of polymer brushes[†]

Thomas Lee,[a‡] **Shaun C. Hendy,**[bc*] **and Chiara Neto**[a]

We have used coarse-grained molecular dynamics simulations to investigate the use of pinned micelles formed by the constrained dewetting of polymer brushes to act as a template for nanoparticle formation. The evaporation of a thin film containing a dissolved solute from a polymer brush was modeled to study the effect of solubility, concentration, grafting density, and evaporation rate on the nucleation and growth of nanoparticles. Control over particle nucleation could be imposed when the solution was dilute enough such that particle nucleation occurred following the onset of constrained dewetting. We predict that nanoparticles with sizes on the order of 1 nm to 10 nm could be produced from a range of organic molecules under experimentally accessible conditions. This method could allow the functionality of organic materials to potentially be imparted onto surfaces without the need for synthetic modification of the functional molecule, and with control over particle size and aggregation, for application in the preparation of surfaces with useful optical, pharmaceutical, or electronic properties.

Polymer brushes, created by tethering polymers by one end onto a surface, offer an elegant and versatile route towards the creation of responsive soft matter surfaces[1]. Changes in the chemical or physical environment of the brush can induce reorganization of the polymer as it swells or collapses[2]. These changes can have dramatic effects on properties of the surface, allowing control over wettability[3,4], lubrication[5], and biocompatibility[6].

Under poor solvent conditions, or when dried out in air, polymer brushes may self-assemble into nanoscale aggregates known as pinned micelles[7–11]. This process is known as constrained dewetting, and results from a competition between the
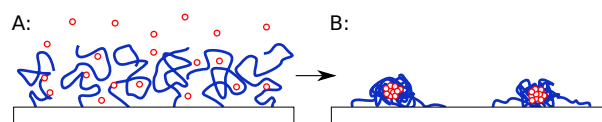

Fig. 1 A: a polymer brush (blue lines) swollen by a a thin film containing a dissolved solute (red circles). B: the surface after the evaporation of the solvent, the precipitation of the solute having been confined by the pinned micelles.

drive to lower the interfacial energy of the system by forming aggregates, and the entropically unfavorable stretching of the tethered polymer chains needed to achieve this arrangement. The patterns formed by constrained dewetting have been observed experimentally using atomic force microscopy, with length scales ranging from 10 nm to 100 nm, controlled by adjusting the polymer grafting density or chain length[12].

In this communication we propose that the patterns formed by constrained dewetting could be used as a template for the formation of molecular nanoparticles on a surface. This method could allow the functionality of organic materials to be imparted onto surfaces without the need for synthetic modification of the functional molecule, and with control over particle size and aggregation. Molecular nanoparticles, the building-blocks of which are molecular species such as small organic molecules, can have many useful optical[13,14], electronic[15], and pharmacological[16] properties. These properties could be used to create novel functional surfaces with potential applications in high-density memory storage[15], light-emitting devices[17], and biological and environmental sensing[18–21].

We have used coarse-grained molecular dynamics simulations and a simple theoretical analysis to study the nucleation of molecular nanoparticles induced by the evaporation of a thin solution film deposited on a low-grafting density polymer brush. We considered the scenario illustrated in Fig. 1. The polymer is initially swollen by the solvent film, which also contains a dissolved solute from which the nanoparticles will be formed. The film evaporates, increasing the concentration of the solute until particles begin to nucleate and grow. At some point during the late stages of the evaporation, constrained dewetting will cause the film to collapse into a "holey layer", then into wormlike aggregates, and finally pinned micelles[11]. We envisage two regimes of behavior: if the collapse of the film occurs prior to the nucleation of stable solute parti-

cles, the solution will be partitioned between the polymer aggregates, as in Fig. 1. As the remaining solvent evaporates the nucleation and growth of solute particles is confined within the individual aggregates. On the other hand, if the collapse of the film occurs after the formation of stable nuclei, no spatial constrain will be imposed on the movement of solute through the film, resulting in uncontrolled growth of large particles. Using molecular dynamics we have tested the effect of changes in the initial concentration of solute, solubility, evaporation rate, and grafting density on the nucleation process in order to investigate the existence of these regimes.

We have made use of a coarse-grained molecular dynamics model implemented in the LAMMPS software package[22]. Snapshots of these simulations are shown in Fig. 2. Four types of particles were modeled: solvent, solute, monomer, and substrate, which will be denoted by the characters 'V', 'U', 'M', and 'B' respectively. The pairwise forces between unbound particles were modeled according to Lennard-Jones potential energy functions of the form:

$$U(r_{ij}) = 4\varepsilon_{ij} \left[(\sigma/r_{ij})^{12} - (\sigma/r_{ij})^6 \right] \tag{1}$$

where r_{ij} is the separation between the particles, σ is the distance parameter, set to unity for all interactions, and ε_{ij} is the energy parameter. All distances have been expressed in terms of the σ parameter, and all energy quantities in terms of the ε parameter for the solvent-solvent interaction ε_{VV}, hereafter denoted ε. Bead-spring polymers were modeled by binding 24 monomers together into a linear chain using a spring-like finitely extensible nonlinear elastic (FENE) potential with commonly used parameters $R_0 = 1.5\sigma$ and $K = 30\varepsilon/\sigma^2$ [23–26].

The substrate was composed of immobile substrate atoms arranged into a square array with a period of 1σ in the xy-plane at the lower z-boundary of the simulation box. Polymer chains were bound by one end to an immobile and noninteracting particle in the plane of the substrate to form a brush with grafting density ρ. These graft-points were arranged on the substrate in a square array with a period $\rho^{-1/2}$ of 8σ, 6σ, or 5σ. In polymer brush simulations, $\varepsilon_{VB} = \varepsilon_{UB} = \varepsilon_{MB} = 0.5\varepsilon$. Control simulations with no polymer used a solvophilic solid substrate with $\varepsilon_{VB} = 1.0\varepsilon$ to more closely match the wetting characteristics of the solvent on the brush. Simulation boxes had a height 30σ and width $(64 \pm 1)\sigma$, such that the width was a multiple of $\rho^{-1/2}$.

Solute particles had a relatively strong attraction to each other to encourage the formation of clusters with low vapor pressure, but not so strong as to prevent them from being dissolved in the solvent-polymer film. Berthelot's combining rule, $\varepsilon_{IJ} = \sqrt{\varepsilon_{II}\varepsilon_{JJ}}$ was used to provide a guide to physically reasonable relative strengths of the interactions between unlike particles of types I and J. Holding $\varepsilon_{MM} = \varepsilon_{VV}$, we found that $\varepsilon_{UU} = 3\varepsilon$ and $\varepsilon_{UV} = \varepsilon_{UM} = 1.73205\varepsilon \approx \sqrt{3}\varepsilon$ provided a system with the required behavior (low solute vapor pressure and nonzero solubility).

After an initial equilibration period, an isothermal evaporation was modeled by periodically removing solvent particles from the vapor-phase region of the simulation box, in the range $25\sigma < z < 30\sigma$. Three different evaporation rates were studied, corresponding to solvent flux densities of $J = 3.33 \times 10^{-4}\sigma^{-2}\tau^{-1}$, $2.00 \times 10^{-4}\sigma^{-2}\tau^{-1}$, and $1.25 \times 10^{-4}\sigma^{-2}\tau^{-1}$, where τ is the Lennard-Jones reduced unit of time. Between 3 to 8 solvent particles were removed at a time, with the time between removals adjusted to bring the actual inverse flux density as close as possible to the target value (within 1%). Simulations were continued for at least 4000τ after the time at which 10 solvent particles were remaining. Polymer brush simulations were run in triplicate, and polymer-free simulations in duplicate, with different seed values used for random generation of initial particle positions and velocities.

Langevin thermostats[27] with target temperature $1\varepsilon/k_B$ were imposed on the monomers and solvent with friction coefficients of $0.1\tau^{-1}$ for the solvent, to compensate for the loss of energy during the evaporation while solvent particles were removed; and $0.01\tau^{-1}$ for the monomers, to compensate for energy released during the condensation of solute once most of the solvent was removed. No thermostat was applied to the solute particles.

We begin by considering the evaporation and nucleation process in the absence of grafted polymer brushes. Only two or three large solute clusters formed when the polymer was not included in the simulation, as seen in the snapshot in Fig. 2A. Simulations containing no polymers were carried out for each combination of evaporation rate, solute concentration, and solubility investigated, with simulation boxes 66σ wide. In many cases the solute clusters encountered each other while moving around the surface, merging into a single large cluster. Additional snapshots from controls are provided in the supplementary information.

Several snapshots taken at various stages during an evaporation of solvent from a polymer brush are shown in Fig. 2B. In snapshot B(i) the polymer was swollen with solvent and the solute completely dissolved. In (ii) the film has begun to break up and constrained dewetting occurs, and in (iii) clusters of solute particles can be seen. At the end of the evaporation in B(iv) several dense solute clusters are observed confined within the polymer aggregates. A clear separation of phases was observed within several of the aggregates seen in Fig. 2B(iv), as the solute particles clustered together while the polymer wrapped around the surface of the nucleus. Some aggregates accumulated only a small amount of solute, which remained in a solution-like state within the polymer.

The formation of solute clusters can be tracked using the weight-averaged cluster mass M_w, shown as a function of time in Fig. 3A for three different evaporation rates. Time is ex-
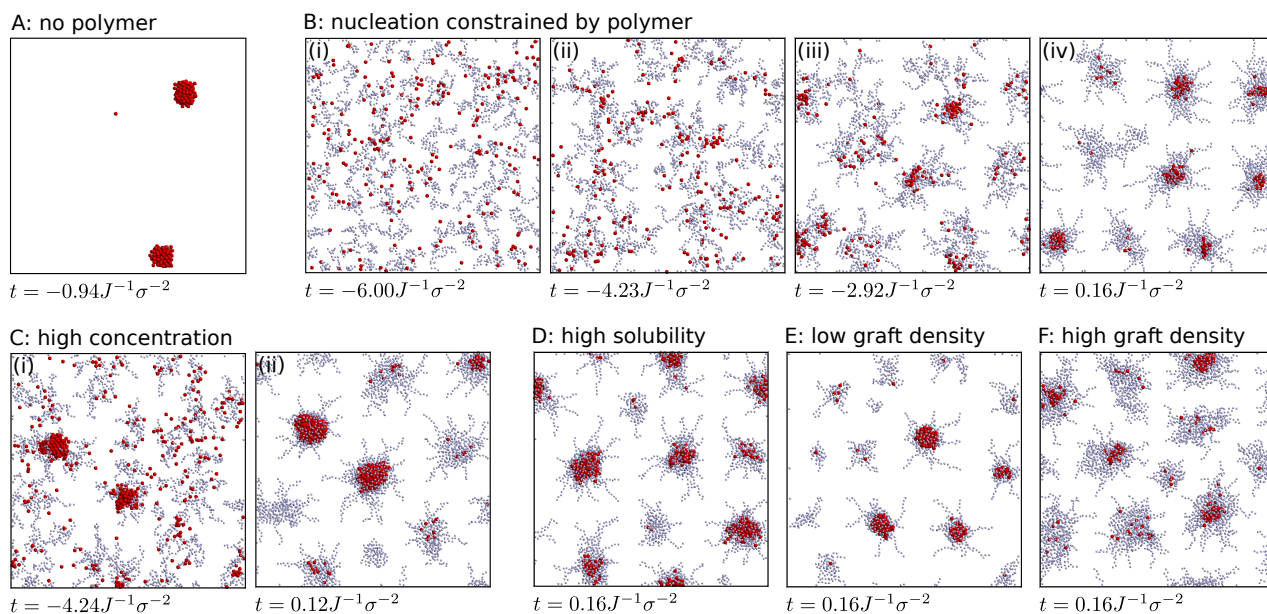
Fig. 2 Top-down snapshots from simulations of nanoparticle formation at a solid substrate. Red and pale blue spheres correspond to solute and monomer particles respectively. Although all particles were the same size, solute and monomer particles are drawn with diameters 1σ and 0.5σ respectively for clarity. Solvent and substrate particles are not drawn. All cases shown correspond to the lowest evaporation rate tested, $J = 1.25 \times 10^{-4}\sigma^{-2}\tau^{-1}$. The snapshot times are relative to the end of the evaporation ($t = 0$) and are multiplied by solvent flux. $\Gamma = 0.05\sigma^{-2}$, $\rho = 2.78 \times 10^{-2}\sigma^{-2}$ and $\varepsilon_{UV} \approx \sqrt{3}\varepsilon$ except where otherwise noted. A: Near the end of a control simulation with in which no polymer was preset. B: Four snapshots taken during an evaporation. C: Two snapshots taken during an evaporation with additional solute ($\Gamma = 0.11\sigma^{-2}$)compared to B. D: The end state of a system with increased solubility compared to C ($\Gamma = 0.11\sigma^{-2}$, $\varepsilon_{UV} = 1.9\varepsilon$). E and F: The end states of systems with $\rho = 1.56 \times 10^{-2}\sigma^{-2}$ and $\rho = 4.00 \times 10^{-2}\sigma^{-2}$ respectively. Additional snapshots and repeats of these simulations are provided in the supplementary material.

pressed relative to the end of the evaporation, $t = 0$. To compare simulations at different evaporation rates, time has been normalized by J^{-1}, the time taken to remove one solvent particle per σ^2. At early times only small clusters of 2-3 solute particles were present, until approximately $t = -4J^{-1}\sigma^{-2}$ when stable nuclei rapidly began to form and grow. The timing of cluster nucleation and growth did not show any trend with respect to the evaporation rate.

The time after which clusters of 10 or more solute particles were always present, t_{10}, is plotted in Fig. 3B as a function of solute surface excess, Γ. This parameter is useful as an approximate guide to the time at which large clusters formed. Changes in the evaporation rate had little or no impact on t_{10}, which decreased approximately linearly with increasing amount of solute in the system. The effect of the earlier nucleation resulting from an increase in Γ can be seen by comparing Fig. 2B and C, with $\Gamma = 0.05\sigma^{-2}$ and $0.11\sigma^{-2}$ respectively. B(ii) and C(i) show systems at the same stage of the evaporation, just as the film had begun to break up. In C(i) nucleation had already occurred, while in B(ii) the solute was still dissolved. The formation of clusters in Fig. 2B was constrained by the polymer aggregation in the initial stages of nucleation, result-

ing in the larger number of smaller clusters in B(iv). The clusters in Fig. 2C had ample time to grow before being separated by the collapsing polymer, resulting in a small number of larger clusters.

The solid red markers in Fig. 3C indicate M_w, normalized by the total mass of solute particles in the system M_{tot}, at the end of the evaporation as a function of the surface excess of solute, Γ. At low values of Γ the average size increased gradually with Γ, but when Γ increased above approximately $8 \times 10^{-2}\sigma^{-2}$, the average size increased rapidly, and was significantly less reproducible between duplicate simulations. This is consistent with the qualitative difference observed in Fig. 2B(iv) and C(ii), suggesting that there is a critical concentration above which control of the cluster formation is lost due to premature nucleation.

The end state of a simulation with increased solute solubility compared to Fig. 2C is shown in Fig. 2D. Solubility was increased by increasing ε_{UV} and ε_{UM} to 1.9ε while holding other parameters constant. For a given solute surface excess, increasing solubility delayed the formation of large clusters to later times, as can be seen in Fig. 3B, in which the open circles represent the high solubility case. In Fig. 2D the nucleation of clusters was delayed until after the break up of the film, such
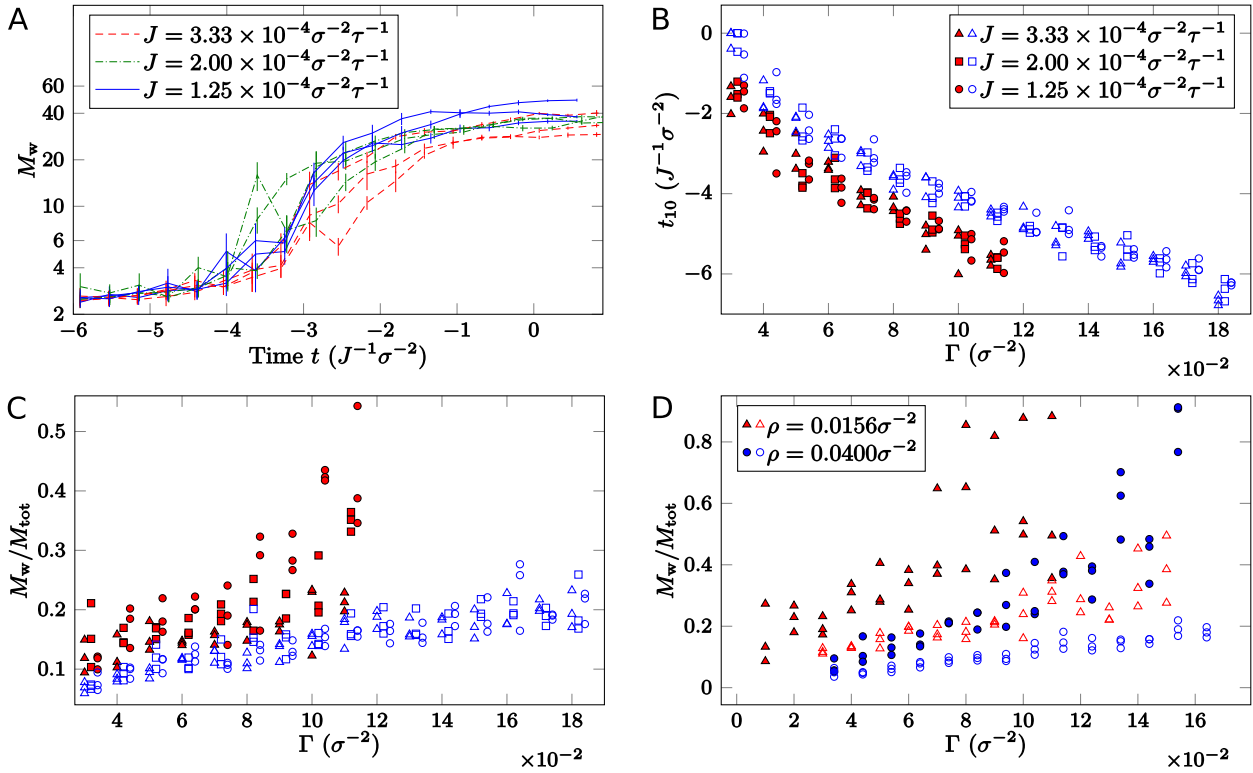
Fig. 3 A: the weight-average mass of solute clusters as a function of time at different evaporation rates with $\rho = 2.78 \times 10^{-2}\sigma^{-2}$, $\Gamma = 0.05\sigma^{-2}$, and $\varepsilon_{UV} \approx \sqrt{3}\varepsilon$. Vertical lines indicate the standard deviation in the mass over an interval of $\Delta t = 0.2J^{-1}\sigma^{-2}$. The legend in B also applies to C. Three repeats are shown for each rate. B, C, and D all display results as a function of the solute surface excess Γ. Filled symbols correspond to $\varepsilon_{UV} \approx \sqrt{3}\varepsilon$ while open symbols correspond to $\varepsilon_{UV} = 1.9\varepsilon$. Squares and circles are offset in the horizontal axis by $0.002\sigma^{-2}$ and $0.004\sigma^{-2}$ respectively for clarity. The errors for individual measurements in C and D were less than 0.02. B: the time after which solute clusters containing 10 particles were always present, t_{10}. C: the weight-average solute cluster mass for $\rho = 2.78 \times 10^{-2}\sigma^{-2}$ at different evaporation rates. D: the weight-average solute cluster mass for $\rho = 2.78 \times 10^{-2}\sigma^{-2}$ at an evaporation rate of $J = 1.25 \times 10^{-4}\sigma^{-2}\tau^{-1}$.

that control was regained over the solute cluster formation compared to Fig. 2C. The effect of the increase in solubility on the final weight-averaged cluster size is shown in Fig. 3C. Compared to the lower solubility simulations, control was maintained over the cluster size at much larger values of Γ. The precipitation of the solute was inhibited until much higher concentrations were reached, at which time the polymer had already formed discrete aggregates.

Different evaporation rates are represented by the different shaped symbols in Fig. 3C. In the range of Γ in which the nucleation was controlled by the constrained dewetting, no effect of the evaporation rate on cluster size was observed. In the lower solubility simulations (red markers), in the regime in which control over nucleation was lost (approximately $\Gamma > 8 \times 10^{-2}\sigma^{-2}$) faster evaporation rates tended to reduce the average cluster size to some degree, possibly a result of the evaporation outpacing the growth of the clusters.

Similar trends were observed at higher and lower grafting density within the pinned-micelle regime. Fig. 2E and F show surface with grafting densities of $1.56 \times 10^{-2}\sigma^{-2}$ and $4.00 \times 10^{-2}\sigma^{-2}$ respectively, and otherwise have the same parameters as Fig. 2B(iv). A similar number of solute clusters formed at the different grafting densities, however the clusters at lower density tended to be larger, as seen quantitatively in Fig. 3D. The presence of a larger amount of polymer at high ρ allowed some of the solute to remain dissolved in the polymer after the solvent was removed. Film break-up occurred later at higher grafting density, but despite this factor controlled nucleation could be achieved at higher Γ due to the greater amount of polymer available to solubilize the solute.

We did not explore the impact of increasing the polymer chain length, due to the larger simulations sizes and timescales which would be required for significantly longer polymers. We expect that increasing the chain length at a given grafting den-
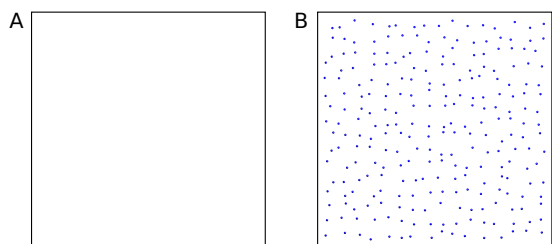
4

Fig. 4 A: Snapshot from a simulation at the end of the evaporation $(t = -1.60 J^{-1}\sigma^{-2})$ with randomized polymer graft points and chain lengths. The parameters were the same as in Fig. 2B except for an increased simulation box width. B: Randomized locations of the polymer graft points. Snapshots from repeated simulations with randomness generated using different seed values are shown in Fig. S17 in the supplementary material.

sity would delay the onset of constrained dewetting and cause the formation of larger features, in a similar manner to increasing the grafting density.

The simulations were repeated in different situations to assess the effect of random order in the grafting points and polydispersity in the chain length on the nucleation and growth of molecular nanoparticles. The same parameters as in Fig. 2B were used, except the simulation box width was increased from 66σ to 96σ for a more complete picture. To make the surface grafting more random, uniform random numbers between -2σ and 2σ were added to both the x and y coordinates of every grafting point. An example of the arrangements of new graft points used is shown in Fig. 4B. The chain length was varied randomly between 22 and 26 units in each brush (to be compared with the original monodisperse chains of 24 units), and five different surfaces were generated. In all cases with the random grafting and polydisperse chains, the final distribution of clusters was very similar to the non-random case, as illustrated in Fig. 4A. Four additional simulations with different random grafting arrangements are shown in Fig. S17 in the supplementary material.

We have performed a simple analysis to predict bounds on the expected nanoparticle size possible using constrained dewetting to control the particle formation. Let $h(t)$ and $\phi_{\text{film}}(t)$ be the height of the film and concentration of solute in the film respectively at a time t, such that $\Gamma = \phi_{\text{film}}(t)h(t)$. Let t_B and t_{nuc} be the time at which film break up and nucleation of solute clusters occurs respectively. Let S be the saturation concentration of the solute in the bulk, and assume that the concentration at which nucleation occurs is given by $\phi_{\text{film}}(t_{\text{nuc}}) = kS$ for a constant $k > 1$.

For the dewetting of the film to constrain the nucleation, the concentration at the break up time needs to be less than that required for nucleation i.e. $\phi_{\text{film}}(t_B) < kS$. The maximum possible Γ to avoid early nucleation can then be derived in terms of

Table 1 Maximum average per-aggregate nanoparticles sizes obtainable near room temperature using a polymer brush which collapses at 10 nm thickness. Initial concentrations are listed for a drop-coating volume of 25 μL/cm^2

solute/solvent	S (mg/mL)	ρ_p (g/cm^3)	A (nm^2)	ϕ_i (μg/mL)	r_p (nm)
glycine/water	227[28]	1.16[28]	10^2	9.1	3.6
			10^4	9.1	17
cortisol/ethanol	15[29]	1.24[30]	10^4	0.6	6.6
β-carotene/THF	10[31]	1.00[28]	10^4	0.4	6.2
C$_{60}$/toluene	3[32]	1.65[33]	10^4	0.12	3.5

the solubility, nucleation coefficient, and film height at the time of breakup:

$$\Gamma < kSh(t_B) \qquad (2)$$

An upper bound on the average particle mass can be obtained by taking the product of the surface excess and the average area per polymer aggregate A. Given the saturation concentration S in terms of mass per unit volume, and the nanoparticle density ρ_p, the average particle radius r_p is constrained by:

$$r_p < \left[(3/4\pi)kSAh(t_B)/\rho_p\right]^{1/3} \qquad (3)$$

The concentration of the initially deposited solution ϕ_i required to obtain maximum surface excess (Eq. 2) depends on the initial film thickness h_i:

$$\phi_i = kSh(t_B)/h_i \qquad (4)$$

Table 1 shows the predicted upper bound on the average r_p per polymer aggregate for several real-world solute-solvent systems. Actual average particle sizes could be larger if some polymer aggregates do not capture a particle, as occurred in Fig. 2B(iv). Nonetheless, these calculations suggest that the synthesis of real nanometer-scale particles with radii on the order of 1 nm to 10 nm could be feasible by the proposed method, with initial concentrations in the range of 0.1-10 ppm.

In conclusion, the simulations and analysis described in this communication suggest that nanopatterns formed by the constrained dewetting of polymer brushes could be used to control the evaporation-induced nucleation and growth of molecular nanoparticles. Control can only be imposed if the solution is dilute enough such that particle nucleation occurs following the onset of constrained dewetting – a condition which depends on the solute surface excess, solubility, and brush grafting density. We predict that nanoparticles with sizes on the order of 1 nm to 10 nm could be produced from a range of organic molecules under experimentally accessible conditions. These concepts might also be applied to nanoparticles formed by more complex chemical pathways, such as the reduction of precursors to form metal or inorganic nanoparticles.

REFERENCES   *REFERENCES*

References

1 J. Rhe and W. Knoll, *J. Macromol. Sci. C*, 2002, **42**, 91–138.

2 F. Zhou and W. T. S. Huck, *Phys. Chem. Chem. Phys.*, 2006, **8**, 3815–3823.

3 M. Motornov, S. Minko, K.-J. Eichhorn, M. Nitschke, F. Simon and M. Stamm, *Langmuir*, 2003, **19**, 8077–8085.

4 A. Sidorenko, S. Minko, K. Schenk-Meuser, H. Duschner and M. Stamm, *Langmuir*, 1999, **15**, 8349–8355.

5 F. T. Limpoco, R. C. Advincula and S. S. Perry, *Langmuir*, 2007, **23**, 12196–12201.

6 M. Welch, A. Rastogi and C. Ober, *Soft Matter*, 2011, **7**, 297.

7 J. Huh, C.-H. Ahn, W. H. Jo, J. N. Bright and D. R. M. Williams, *Macromolecules*, 2005, **38**, 2974–2980.

8 S. K. Pattanayek, T. T. Pham and G. G. Pereira, *J. Chem. Phys.*, 2005, **122**, 214908–14.

9 K. G. Soga, G. Hong and M. J. Zuckermann, *EPL*, 1995, **29**, 531.

10 D. Williams, *J. Phys. II*, 1993, **3**, 1313–1318.

11 T. Lee, S. C. Hendy and C. Neto, *Macromolecules*, 2013, **46**, 6326–6335.

12 V. Koutsos, E. W. van der Vegte, E. Pelletier, A. Stamouli and G. Hadziioannou, *Macromolecules*, 1997, **30**, 4719–4726.

13 Z. Zhao, S. Chen, X. Shen, F. Mahtab, Y. Yu, P. Lu, J. W. Y. Lam, H. S. Kwok and B. Z. Tang, *Chem. Commun.*, 2010, **46**, 686.

14 E. I. Maltsev, D. A. Lypenko, V. V. Bobinkin, A. R. Tameev, S. V. Kirillov, B. I. Shapiro, H. F. M. Schoo and A. V. Vannikov, *Appl. Phys. Lett.*, 2002, **81**, 3088.

15 S. Rath, M. Heilig, H. Port and J. Wrachtrup, *Nano Letters*, 2007, **7**, 3845–3848.

16 R. H. Muller and C. M. Keck, *J. Biotechnol*, 2004, **113**, 151–170.

17 A. Patra, C. G. Chandaluri and T. P. Radhakrishnan, *Nanoscale*, 2012, **4**, 343.

18 L. Wang, T. Xia, L. Wang, H. Chen, L. Dong and G. Bian, *Microchimica Acta*, 2005, **149**, 267–272.

19 L. Wang, L. Wang, L. Dong, G. Bian, T. Xia and H. Chen, *Spectrochim. Acta A*, 2005, **61**, 129–133.

20 L. Wang, L. Wang, T. Xia, L. Dong, G. Bian and H. Chen, *Anal. Sci.*, 2004, **20**, 1013–1017.

21 H. Li and H. Yan, *J. Phys. Chem. C*, 2009, **113**, 7526–7530.

22 S. Plimpton, *J of Comput. Phys.*, 1995, **117**, 1–19.

23 K. Kremer and G. S. Grest, *J. Chem. Phys.*, 1990, **92**, 5057–5086.

24 K. Binder, T. Kreer and A. Milchev, *Soft Matter*, 2011, **7**, 7159–7172.

25 M. Müller, C. Pastorino and J. Servantie, *Comput. Phys. Commun.*, 2009, **180**, 600–604.

26 C. Pastorino, T. Kreer, M. Muller and K. Binder, *Phys. Rev. E*, 2007, **76**, 026706.

27 W. van Gunsteren and H. Berendsen, *Mol. Phys.*, 1982, **45**, 637–647.

28 *CRC Handbook of Chemistry and Physics*, ed. W. M. Haynes, CRC press, 94th edn., 2013.

29 Merck, *The Merck Index. [online]*, Merck & Co., Inc, 2013.

30 T. A. Hagen and G. L. Flynn, *J. Pharm. Sci.*, 1983, **72**, 409–414.

31 N. E. Craft and J. H. Soares, *J. Agr. Food Chem.*, 1992, **40**, 431–434.

32 K. N. Semenov, N. A. Charykov, V. A. Keskinov, A. K. Piartman, A. A. Blokhin and A. A. Kopyrin, *J. Chem. Eng. Data*, 2010, **55**, 13–36.

33 W. Krátschmer, L. D. Lamb, K. Fostiropoulos and D. R. Huffman, *Nature*, 1990, **347**, 354–358.